

Strong anharmonicity-assisted low lattice thermal conductivities and high thermoelectric performance in double-anion Mo_2AB_2(A=S, Se, Te; B=Cl, Br, I) semiconductors

Haijun Liao(廖海俊) Le Huang(黄乐), Xing Xie(谢兴), Huafeng Dong(董华锋), Fugen Wu(吴福根) Zhipeng Sun(孙志鹏), and Jingbo Li(李京波)
Citation: Chin. Phys. B, 2023, 32 (**10**): 107304. DOI: 10.1088/1674-1056/ace314

Journal homepage: http://cpb.iphy.ac.cn; http://iopscience.iop.org/cpb

What follows is a list of articles you may be interested in

Nonlinear current response and electric quantum oscillations in the Dirac semimetal Cd_3As_2

Hao-Nan Cui(崔浩楠), Ze-Nan Wu(吴泽南), Jian-Kun Wang(王建坤), Guang-Yu Zhu(祝光宇), Jia-Jie Yang(杨佳洁), Wen-Zhuang Zheng(郑文壮), Zhi-Min Liao(廖志敏), Shuo Wang(王硕), Ben-Chuan Lin(林本川), and Dapeng Yu(俞大鹏)
Chin. Phys. B, 2023, 32 (**8**): 087306. DOI: 10.1088/1674-1056/acd9c5

Room temperature quantum anomalous Hall insulator in honeycomb lattice, $RuCS_3$, with large magnetic anisotropy energy

Yong-Chun Zhao(赵永春), Ming-Xin Zhu(朱铭鑫), Sheng-Shi Li(李胜世), and Ping Li(李萍)
Chin. Phys. B, 2023, 32 (**5**): 057301. DOI: 10.1088/1674-1056/aca396

Thermoelectric signature of Majorana zero modes in a T-typed double-quantum-dot structure

Cong Wang(王聪) and Xiao-Qi Wang(王晓琦)
Chin. Phys. B, 2023, 32 (**3**): 037304. DOI: 10.1088/1674-1056/ac92d3

Enhanced thermoelectric properties in two-dimensional monolayer Si_2BN by adsorbing halogen atoms

Cheng-Wei Wu(吴成伟), Changqing Xiang(向长青), Hengyu Yang(杨恒玉), Wu-Xing Zhou(周五星), Guofeng Xie(谢国锋), Baoli Ou(欧宝立), and Dan Wu(伍丹)
Chin. Phys. B, 2021, 30 (**3**): 037304. DOI: 10.1088/1674-1056/abd163

Strategies for optimizing the thermoelectricity of PbTe alloys

Jinze Zhai(翟近泽), Teng Wang(王腾), Hongchao Wang(王洪超), Wenbin Su(苏文斌), Xue Wang(王雪), Tingting Chen(陈婷婷), Chunlei Wang(王春雷)
Chin. Phys. B, 2018, 27 (**4**): 047306. DOI: 10.1088/1674-1056/27/4/047306

Strong anharmonicity-assisted low lattice thermal conductivities and high thermoelectric performance in double-anion Mo_2AB_2 (A = S, Se, Te; B = Cl, Br, I) semiconductors

Haijun Liao(廖海俊)[1], Le Huang(黄乐)[1,2,†], Xing Xie(谢兴)[4], Huafeng Dong(董华锋)[2,3], Fugen Wu(吴福根)[1], Zhipeng Sun(孙志鹏)[1,‡], and Jingbo Li(李京波)[5,§]

[1] *School of Materials and Energy, Guangdong University of Technology, Guangzhou* 510006, *China*
[2] *Guangdong Provincial Key Laboratory of Information Photonics Technology, Guangdong University of Technology, Guangzhou* 510006, *China*
[3] *School of Physics and Optoelectronic Engineering, Guangdong University of Technology, Guangzhou* 510006, *China*
[4] *School of Physics and Electronics, Hunan Key Laboratory for Super-microstructure and Ultrafast Process, Central South University, Changsha* 410083, *China*
[5] *College of Optical Science and Engineering, Zhejiang University, Hangzhou* 310027, *China*

(Received 27 March 2023; revised manuscript received 7 June 2023; accepted manuscript online 30 June 2023)

The thermoelectric properties of layered Mo_2AB_2 (A = S, Se, Te; B = Cl, Br, I) materials are systematically investigated by first-principles approach. Soft transverse acoustic modes and direct Mo d–Mo d couplings give rise to strong anharmonicities and low lattice thermal conductivities. The double anions with distinctly different electronegativities of Mo_2AB_2 monolayers can reduce the correlation between electron transport and phonon scattering, and further benefit much to their good thermoelectric properties. Thermoelectric properties of these Mo_2AB_2 monolayers exhibit obvious anisotropies due to the direction-dependent chemical bondings and transport properties. Furthermore, their thermoelectric properties strongly depend on carrier type (n-type or p-type), carrier concentration and temperature. It is found that n-type Mo_2AB_2 monolayers can be excellent thermoelectric materials with high electric conductivity, σ, and figures of merit, ZT. Choosing the types of A and B anions of Mo_2AB_2 is an effective strategy to optimize their thermoelectric performance. These results provide rigorous understanding on thermoelectric properties of double-anions compounds and important guidance for achieving high thermoelectric performance in multi-anion compounds.

Keywords: thermoelectricity, anharmonicity, lattice thermal conductivity, anisotropy, first-principles calculations

PACS: 73.50.Lw, 63.22.–m, 73.22.–f, 72.10.–d **DOI:** 10.1088/1674-1056/ace314

1. Introduction

For the past few years, the problem of the fossil fuel crisis and climatic issues has become more and more serious, and thermoelectricity (TE) materials have been widely studied due to their low-pollution-environmental-friendly application.[1–5] The energy conversion efficiency in TE technology is mainly by the dimensionless figure of merit of the employed material. It is calculated as $ZT = S^2\sigma T/\kappa$, where S is the Seebeck coefficient, σ is the electric conductivity, κ is the thermal conductivity including charge carrier (κ_e) and lattice (κ_l) contributions, T is the absolute temperature.[6] Several excellent reviews describe the rules for enhancing TE efficiency by energy-band engineering,[7–10] interfacial engineering,[11] impurity doping,[12–14] mosaic microstructure,[15] and component alloying.[16–18]

The key difficulty in obtaining high TE property with high σ and low κ lies in reduce the correlation between electron transport and phonon scattering, which is usually hard to carry out. From the definition of the thermoelectricity figure of merit, it is clear that material with high electric conductivity and Seebeck coefficient or low thermal conductivity can actually be an ideal TE material. Whereas, using a straightforward way to get high TE performance is a difficult work because of these strong coupling of properties above. It is demonstrated that some special and complex crystal structures will reduce thermal conduction without decreasing electronic transport.[19,20] The two-dimensional (2D) SnSe can get $ZT \approx 4.31$ at 500 K, through properly adjusting interlayer distance to restrain thermal transport and to improve electric transport.[21] Excellent TE properties were achieved in doped clathrate compounds, in which σ and κ are weakly correlated due to the weak coupling between guest atoms and the clathrate framework.[22] Theoretical and experimental works demonstrated that weak coupling between σ and κ requires low-frequency phonon vibrations, resulting in amplified asymmetric atomic vibrations and enhanced anharmonicities. This strategy was employed in many semiconductors, such as α-MgAgSb[23] and Cu_3SbSe_3[24] to obtain high TE

†Corresponding author. E-mail: huangle@gdut.edu.cn
‡Corresponding author. E-mail: zpsunxj@163.com
§Corresponding author. E-mail: jbli@zju.edu.cn

© 2023 Chinese Physical Society and IOP Publishing Ltd

performance.

It is established that low-frequency phonon vibrations with strong anharmonicities usually appear in TE materials with complex structures which usually exhibit bonding heterogeneity transport anisotropy.[25,26] Double-anion semiconductors have been proved to be promising TE materials with complex structures. As a typical double-one, Bi_2O_2Se, actually achieves higher carrier transport and lower thermal conductivity compared to Bi_2Se_3.[27,28] $Al_2A_2Se_2$ (A = Cl, Br, I) exhibit anisotropic thermal conductivities due to the direction-dependent Al–Se bonding.[29] Monolayer $In_2Cl_2O_2$[30] and $Ga_2I_2S_2$[31] show strong anisotropies in their power factors and low-level thermal conductivity.

As another class of double-anion semiconductors, transition metal sulfide halides, TM_2AB_2 (TM = Mo, W; A = S, Se, Te; B = Cl, Br, I) have been explored to have excellent anisotropic electric transport properties.[32] The rather complex crystal structures and low lattice symmetry of these materials make them promising TE semiconductors. Further studies to explore the TE properties of TM_2AB_2 and the underlying mechanism are in much desire. The unique natures with respect to other aforementioned double-anion materials in the TE properties of TM_2AB_2 are also far from explored.

In this context, we studied the structural and electronic properties of layered Mo_2AB_2 (A = S, Se, Te; B = Cl, Br, I) materials to explore their promising TE performance by first-principles approach. Excellent TE properties with high σ and low κ are revealed. The low κ is attributed to soft phonon modes with strong anharmonicity. Direct Mo–Mo couplings further reduce the lattice thermal conductivities and increase the anharmonicities by introducing low-frequency phonon modes. TE properties of these Mo_2AB_2 monolayers exhibit obvious anisotropies due to the direction-dependent chemical bondings and transport properties. The double anions with distinct electronegativities of Mo_2AB_2 monolayers benefit much to their good TE properties. These results provide a theoretical understanding on the TE properties of double-anion compounds, and provide instruction to realize high TE performance in Mo_2AB_2 semiconductors by selecting the type of anions and regulating carrier type and concentration.

2. Methodology

Structural optimization and total energy calculations are performed by first-principles methods as implemented in the Vienna *ab initio* simulation package (VASP)[33] with the projector augmented-wave method.[34] Electronic exchange–correlation is described by the Perdew–Burke–Ernzerhof (PBE) functional within the generalized gradient approximation (GGA).[35] The cutoff energy of the planewave basis is set as 400 eV. A $8\times4\times1$ k-point mesh in the first Brillouin zone (BZ) is used in structural relaxation and total energy calculations. All the structures are fully optimized with a force tolerance of 10^{-6} eV/Å on each atom. A vacuum layer larger than 15 Å along the out-of-plane direction is adopted to eliminate interactions between adjacent images. Detailed features of chemical bonding of Mo_2AB_2 are explored by calculating the crystal orbital Hamiltonian populations (COHPs).[36] Through post-processing the data from VASP calculations, projected COHP (–pCOHP) results for chemical bondings can be obtained by using LOBSTER software.[37]

Accurate electronic structures are calculated by using hybrid Heyd–Scuseria–Ernzerhof (HSE06) functional with the default mixing parameter of 0.20, as implemented in PWmat package.[38–40] The phonon dispersion of all the employed systematically calculated by density functional perturbation theory method[41] with the second-order interatomic force constants (IFCs) considered, as implemented in PHONOPY software.[42,43] The third-order IFCs are obtained by resolving the irreducible set of atomic displacements with assist of the THIRDORDER.PY script.[44] A $2\times1\times1$ supercell with the k-grid mesh of $2\times2\times1$ is used in the second- and third-order IFCs calculations with the energy and force convergence criteria of 10^{-8} eV and 10^{-6} eV/Å, respectively. The cut-off radius of the nearest interaction is set as 1.40 nm in the third-order IFCs calculations. All the parameters related to the third-order IFCs calculations are tested for convergence, as shown in Fig. S3 in supporting information.

Based on the second- and third-order interatomic force constants, the temperature-dependent lattice thermal conductivities (κ_l) are obtained by ShengBTE software package[44] through solving the linearized phonon Boltzmann transport equation (BTE)

$$\kappa_{\mathrm{L}}^{ab}=\frac{1}{k_{\mathrm{B}}T^2\Omega N}\sum_{\lambda}f_0(f_0+1)(\hbar\omega_\lambda)^2\upsilon_\lambda^a F_\lambda^b, \tag{1}$$

where k_{B} stands for the Boltzmann constant, and T is absolute temperature. $\hbar$ is the reduced Planck constant. f_0 stands for the Bose–Einstein distribution. Ω is defined as the volume of the unit cell and N is the number of Gamma-centered k-points, $N=10\times10\times1$ in first BZ for this work. The ω_λ and υ_λ are the angular frequency and phonon group velocity of the phonon mode λ, respectively. The component of the phonon mean free path (MFP) along the b direction is represented as F_λ^b.

The electric transport properties as functions of carrier concentration and temperature are calculated using BOLTZTRAP code.[45] The electric conductivity σ and Seebeck coefficient S are expressed as

$$\sigma=e^2\int \mathrm{d}\varepsilon\left(-\frac{\partial f_0}{\partial\varepsilon}\right)\sum_k \upsilon_k\upsilon_k\tau_k, \tag{2}$$

$$S=\frac{ek_{\mathrm{B}}}{\sigma}\int \mathrm{d}\varepsilon\left(-\frac{\partial f_0}{\partial\varepsilon}\right)\frac{\varepsilon-\eta}{k_{\mathrm{B}}T}\sum_k \upsilon_k\upsilon_k\tau_k, \tag{3}$$

where f_0 represents the equilibrium Fermi distribution function. η is the chemical potential. τ_k and υ_k stand for the carrier relaxation time and group velocity of an electron at the k state, respectively. The deformation potential (DP) theory is employed to calculate the carrier mobility and carrier relaxation time, and the details of these calculations are given in supporting information.

3. Results and discussion

Bulk Mo_2AB_2 (A = S, Se, Te; B = Cl, Br, I) holds space group of *Pmma* with layered structure. Figure 1(a) shows the crystal structure and the first BZ of monolayer Mo_2AB_2. The unitcell of monolayer Mo_2AB_2 contains total 30 atoms due to its relative low symmetry in comparison with transition metal dichalcogenides. The in-plane lattice constants of monolayer Mo_2AB_2 are listed in Table S1. Due to the orthogonal crystal structures, these monolayers present obvious anisotropic features in their structural and transport properties.[32]

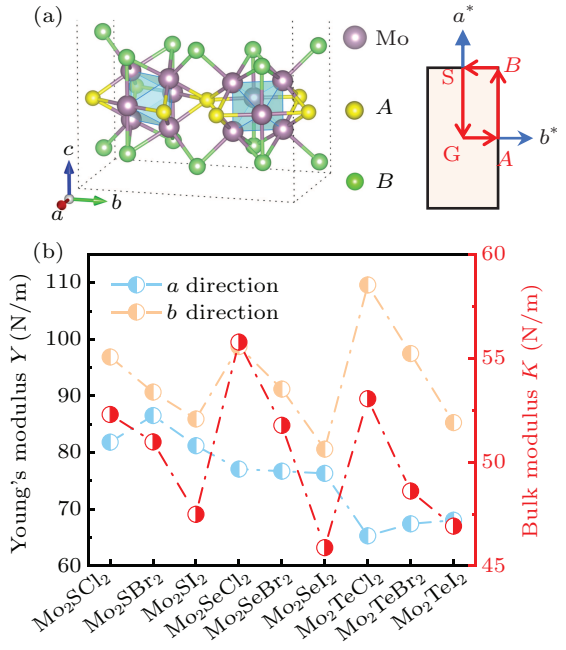


Fig. 1. (a) Crystal structures of Mo_2AB_2 monolayer. The interlayer direction is redefined to along the c direction. Its first Brillouin zone with high-symmetry points labeled is also plotted here. (b) Calculated Young's modulus (blue and orange points), Y, and bulk modulus (red points), K, of MoAB_2 monolayers.

To evaluate the thermodynamic stability of these monolayers, the phonon dispersions are calculated in Fig. 2. It is found that monolayer Mo_2SB_2 (B = Cl, Br, I), Mo_2SeCl_2, and Mo_2SeBr_2 show no imaginary frequencies in their phonon spectra, indicating they are dynamically stable. While phonon dispersions of other four Mo_2AB_2 monolayers employed in this work present an imaginary frequency at S (0.5 0.0 0.0) point. It is found that heavier A and B anions tend to reduce the dynamic stability of Mo_2AB_2 monolayer. Additionally, for a given vibration mode, its phonon frequency decreases as the atomic masses of A and B increases. Consequently, the speed of sound also decreases with the atomic number of A and B ions, following the inverse proportionality between the speed of sound and the atomic mass.

Exploring the mechanical properties of a material is usually helpful to evaluate its thermal transport properties. In Fig. 1(b) and Table S1, elastic constants, C_{11}, C_{22}, C_{12}, C_{66} and associated Young's modulus Y, and bulk modulus K, are calculated. The elastic constants of all the structures satisfy the thermostable rules in orthogonal symmetry ($C_{11} > 0$ & $C_{22} > 0$ & $C_{66} > 0$ & $C_{11} \cdot C_{22} > C_{12}^2$). Our results indicate that all the Mo_2AB_2 monolayers exhibit good mechanical stability with moderate Y and K values.[32] High anisotropies are observed in their Young's modulus due to their anisotropic characters of chemical bondings. Especially, as the atomic sizes of A and B atoms increase, the anisotropies of mechanical properties are enhanced. Detailed analysis of their crystal structures can provide clear evidence for the increasing anisotropy. Specifically, it is observed that the Mo–A bondings exhibit high-covalency characters along the b direction, which results in the larger Young's modulus along this direction than along the a direction. As a result, the acoustic velocity and associated thermal conductivity along the b direction is expected to be higher than the a direction. Furthermore, it is noted that these Mo_2AB_2 monolayers have low bulk modulus about 50 N/m. So relative weak chemical bonding is expected in Mo_2AB_2 monolayers. It can be assumed that these Mo_2AB_2 monolayers should exhibit low thermal conductivities due to their soft lattices with high ionic bondings.

From the phonon dispersions in Fig. 2, we also found that acoustic velocities corresponding to transverse acoustic (TA), longitudinal acoustic (LA) and the third acoustic (ZA) modes are different from each other. It should be mentioned that all these three acoustic modes exhibit weak dispersions in the image, resulting in low acoustic velocities. Furthermore, there is no energy gap between acoustic modes and low-frequency optical phonon modes, indicating the existence of strong phonon scattering between low-frequency optical modes and acoustic modes. These results reveal that there exists relative strong three-phonon scattering in Mo_2AB_2 monolayers. Consequently, lattice thermal conductivity can be restricted by this three-phonon scattering restrains the thermal conductivity, severely enhancing the thermoelectric performance of these materials.

Electronic properties and orbital coupling characters are intimately related to the thermoelectric properties of a material. From the electronic band structures in Fig. S1, it is found that all Mo_2AB_2 monolayers have direct bandgaps at the S (0.50.00.0) point of the first BZ (Fig. 1(a)). Accurate electronic structures are obtained by using HSE06 functional

method. As shown in Fig. 3(a), the bandgap of Mo_2AB_2 monolayer shows significant dependence on the atomic number of *A* and weak dependence on that of *B* anions. Further evidence can be obtained from their projected density of states (PDOS) in Fig. S2. Compared to chalcogenide *A* ions, *B* ions have major contributions to conduction band states. The VBM states are mainly composed of Mo 4d and *A* p orbitals. Additionally, Mo_2AB_2 monolayers are expected to have similar magnitude of Seebeck coefficients due to their rather similar general features in their electronic structures near the Fermi level. In Fig. 3(a), energy positions of bandedge states, the VBM and CBM states, of these Mo_2AB_2 monolayers with respect to the vacuum level are calculated on the HSE06 level. For given *A* in Mo_2AB_2, energy positions of the VBM and CBM increase with the atomic number of *B*. As the atomic number of *A* increases, the VBM states shift up, but inverse trend for CBM state. This is mainly attributed to the increasing atomic level of *B* (or *A*) p orbitals.

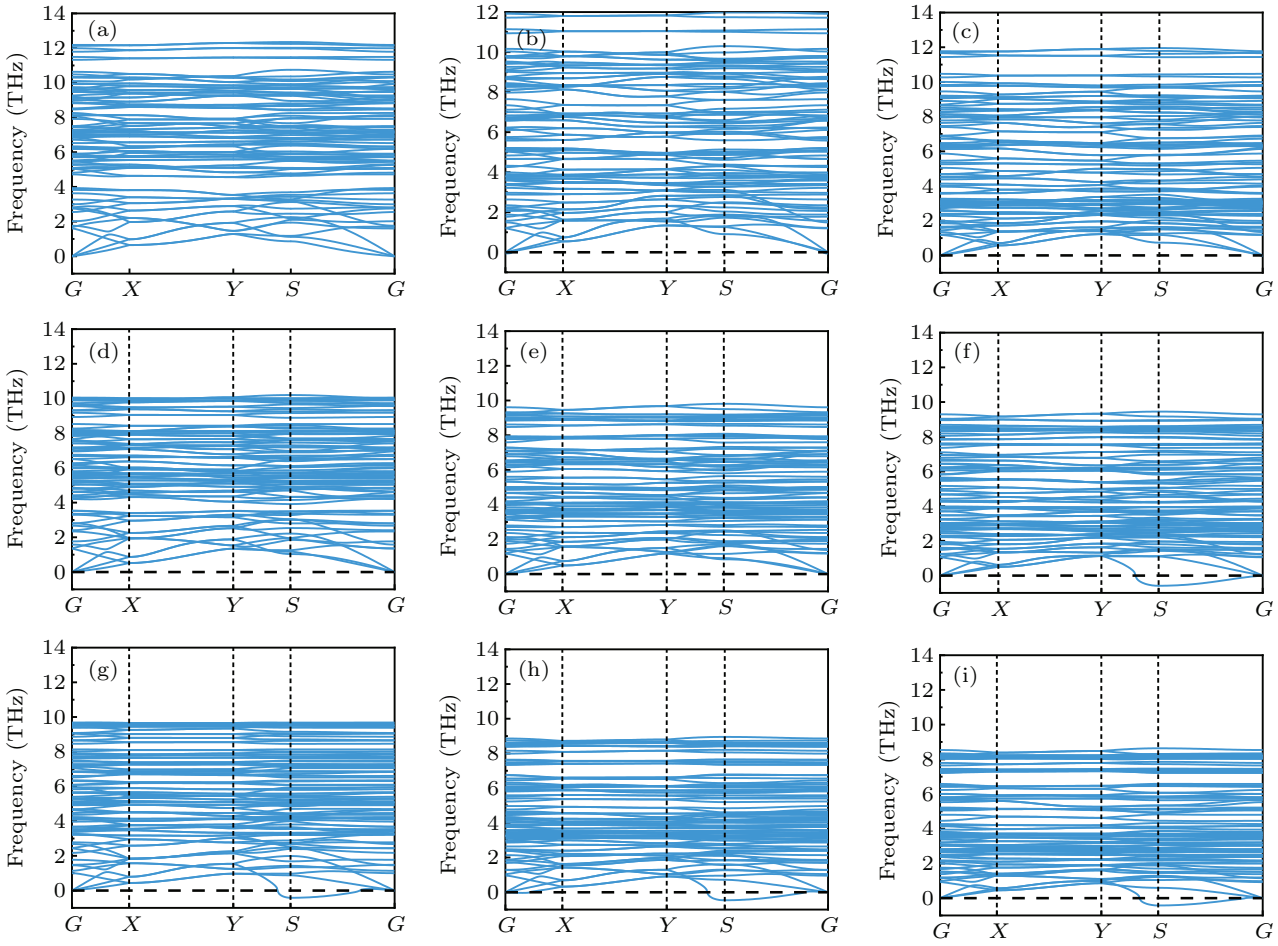


Fig. 2. The phonon band structure of monolayer (a) Mo_2SCl_2, (b) Mo_2SBr_2, (c) Mo_2SI_2, (d) Mo_2SeCl_2, (e) Mo_2SeBr_2, (f) Mo_2SeI_2, (g) Mo_2TeCl_2, (h) Mo_2TeBr_2, (i) Mo_2TeI_2.

It is known that the electric and thermal conductivities as well as associated thermoelectric properties severely depend on the chemical bonding characters of the bandedge states. To reveal the chemical bonding characters of the bandedge states, the VBM and CBM states, of Mo_2AB_2 monolayers, Mo_2SCl_2 monolayer is taken as an example to calculate the –pCOHP In Fig. 3(b). It can be seen that the CBM state is mainly composed by the antibonding states of Mo–Mo, Mo–S, and Mo–Cl bonds. While the VBM state is formed by bonding state of Mo–Mo bond and antibonding states of Mo–S and Mo–Cl bonds. With increasing atomic numbers of *A* or *B*, weakened antibonding coupling of Mo d–Mo d orbitals tend to reduce the energy positions of the CBM state. As given in Tables 1 and 2, carrier effective masses, m_e and m_h of Mo_2AB_2 monolayer decrease with increasing atomic number of *A* due to the enhanced band dispersion. While from Mo_2ACl_2, Mo_2ACl_2, to Mo_2AI_2, m_h and m_e along the *b* direction increase, which can be ascribed to the decreasing electronegativity from Cl, Br to I. It has been proved that this d–d coupling is responsible for the high carrier mobility and strong anisotropies in mechanical and electronic properties.[32] Of more importance is that the coupled Mo–Mo dimers can enhance the anharmonicity and the scattering of acoustic phonons, which should be beneficial to achieve low lattice thermal conductivity. This unique d–d coupling can be essential to the thermoelectric properties of Mo_2AB_2 monolayer.

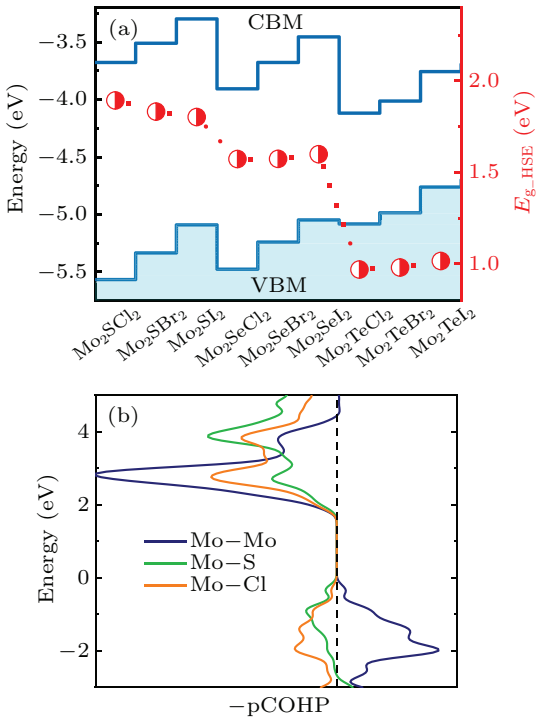


Fig. 3. (a) Energy positions of bandedge states and bandgaps of Mo_2AB_2 monolayers. (b) The –pCOHP analysis for the Mo–Cl, Mo–S, and Mo–Mo bondings in Mo_2SCl_2 monolayer. –pCOHP values on the left side of the dashed line indicate the anti-bonding states and the those on the right side mean the bonding states.

Table 1. The calculated carrier effective mass m^*, carrier mobility μ (in units $cm^2/(V{\cdot}s)$) and carrier relaxation time τ (in unit ps) along the a and b directions of Mo_2AB_2 monolayers for electrons. m_0 is the static mass of electron.

Materials	Electron					
	μ_a	μ_b	τ_a	τ_b	m_a^*/m	m_b^*/m
Mo_2SCl_2	17045.51	591.47	4.11	0.15	0.99	1.03
Mo_2SBr_2	9220.26	620.21	4.25	0.39	0.81	1.11
Mo_2SI_2	10158.50	618.263	4.11	0.44	0.71	1.26
Mo_2SeCl_2	228.37	1187.15	0.11	0.14	0.82	0.21
Mo_2SeBr_2	463.11	1143.91	0.18	0.16	0.70	0.25
Mo_2SeI_2	–	–	–	–	1.02	0.65
Mo_2TeCl_2	978.52	5012.35	0.34	0.29	0.61	0.10
Mo_2TeBr_2	1187.29	4019.18	0.36	0.25	0.54	0.11
Mo_2TeI_2	1868.24	3074.72	0.51	0.24	0.47	0.14

Insights into electrical transport properties of Mo_2AB_2 can be obtained from carrier mobility (μ), carrier relaxation time (τ), and effective mass (m^*) in Table 1 and Table 2. Our results show that electrons in Mo_2SB_2 and holes in Mo_2SeB_2 and Mo_2TeB_2 have ultra-high carrier mobilities along the a direction and long carrier relaxation time due the weak LA scattering. We confirmed this by calculating the deformation constants in the LA mode, as given in Table S2 in supporting information. Weak LA scattering in Mo_2AB_2 monolayers results in large carrier relaxation time and high carrier mobility, especially along the a direction. According to Eqs. (2) and (3), Mo_2AB_2 monolayers can achieve high electric conductivity and large Seebeck coefficient due to the high carrier relaxation time. Our results indicate that excellent charge transport property and strong anisotropy widely exist in these Mo_2AB_2 semiconductors, which indicates that Mo_2AB_2 can be utilized as optoelectronic and thermoelectricity devices.

Table 2. The m^*, μ (in unit $cm^2/(V{\cdot}s)$), and τ (in unit ps) of Mo_2AB_2 monolayers for holes in two directions. m_0 is the static mass of electron.

Materials	Hole					
	μ_a	μ_b	τ_a	τ_b	m_a^*/m	m_b^*/m
Mo_2SCl_2	171.55	1051.64	0.12	0.13	1.25	0.22
Mo_2SBr_2	217.29	868.96	0.15	0.12	1.17	0.25
Mo_2SI_2	221.75	802.29	0.18	0.15	1.40	0.32
Mo_2SeCl_2	2921.19	3102.58	1.33	0.32	0.80	0.18
Mo_2SeBr_2	1869.64	2580.88	0.83	0.29	0.78	0.19
Mo_2SeI_2	–	–	–	–	0.83	0.22
Mo_2TeCl_2	34075.30	11156.61	8.33	0.63	0.43	0.10
Mo_2TeBr_2	25726.60	9428.11	6.29	0.54	0.43	0.10
Mo_2TeI_2	42791.10	7072.27	10.95	0.44	0.45	0.11

As a typical Mo_2AB_2 monolayer, Mo_2SCl_2 monolayer is employed to investigate its thermoelectric performance to provide a comprehensive understanding on the physics of thermoelectric properties of Mo_2AB_2 monolayers. In Fig. 4, the direction-dependent electrical transport properties of Mo_2SCl_2 monolayer at different temperatures and carrier concentrations are calculated by solving the BTE, implemented in the BOLTZTRAP code.[45] We find in Figs. 4(a) and 4(b) that the Seebeck coefficient S shows no obvious direction-dependent variations and decreases with carrier concentration. At 300 K with carrier concentration of 10^{12} cm^{-2}, $|S|$ of Mo_2SCl_2 monolayer for n-type are 363 $\mu V{\cdot}K^{-1}$ in the a direction and 322 $\mu V{\cdot}K^{-1}$ in the b direction, which are much larger than those of SnTe (< 150 $\mu V{\cdot}K^{-1}$ for p-type carriers)[46] and PbTe (< 120 $\mu V{\cdot}K^{-1}$ for p-type carriers).[47]

Figures 4(c) and 4(d), show that the calculated electric conductivities, σ, of Mo_2SCl_2 monolayer increase with the carrier concentration, n. More importantly, for p-type conductivity, σ along the b direction is much higher than that along the a direction due to the smaller hole effective mass along the b direction. While in the case of n-type conductivity, electron mobility along the a direction is higher than that along the b direction. Low scattering rates of the LA mode to electrons give rise to the high electric conductivity, especially in Mo_2SCl_2 along the a direction.

It should be mentioned that electronic thermal conductivity, κ_e, of these monolayers does not vary by much due to their similar general features in their chemical bonding, following the Wiedemann–Franz law[48] ($\kappa_e = L\sigma T$, where L is the Lorenz factor which can be estimated from the Seebeck coefficient, and $L = 2.45 \times 10^{-8}$ $W{\cdot}\Omega{\cdot}K^{-2}$. In Figs. 4(e) and 4(f), the carrier thermal conductivities, κ_e of Mo_2SCl_2 are calculated. It is revealed that κ_e of Mo_2SCl_2 monolayer as n-type or p-type semiconductor exhibit similar variations as functions of n. It is found that along the a direction, σ and κ_e of n-type Mo_2SCl_2 are significantly larger than corresponding values of

p-type one. These results are in line with the results of carrier mobility and carrier relaxation time in Tables 1 and 2.

In Figs. 4(g) and 4(h), the power factor ($PF = S^2\sigma$) values of Mo_2SCl_2 monolayer as n-type or p-type semiconductor are calculated. Along the *b* direction, *PF* values of n-type and p-type Mo_2SCl_2 monolayers exhibit rather similar variations with carrier concentrations with the maximum value of 8.86 mW/mK^2. Along the *a* direction, Mo_2SCl_2 monolayer has much higher *PF* values as an n-type semiconductor than a p-type one due to the larger Seebeck coefficient and electric conductivity along this direction. The maximum *PF* value of n-type Mo_2SCl_2 monolayer at 300 K is 73.85 mW/mK^2 along the *a* direction. The high *PF* value implies that Mo_2SCl_2 will have excellent thermoelectric performance.

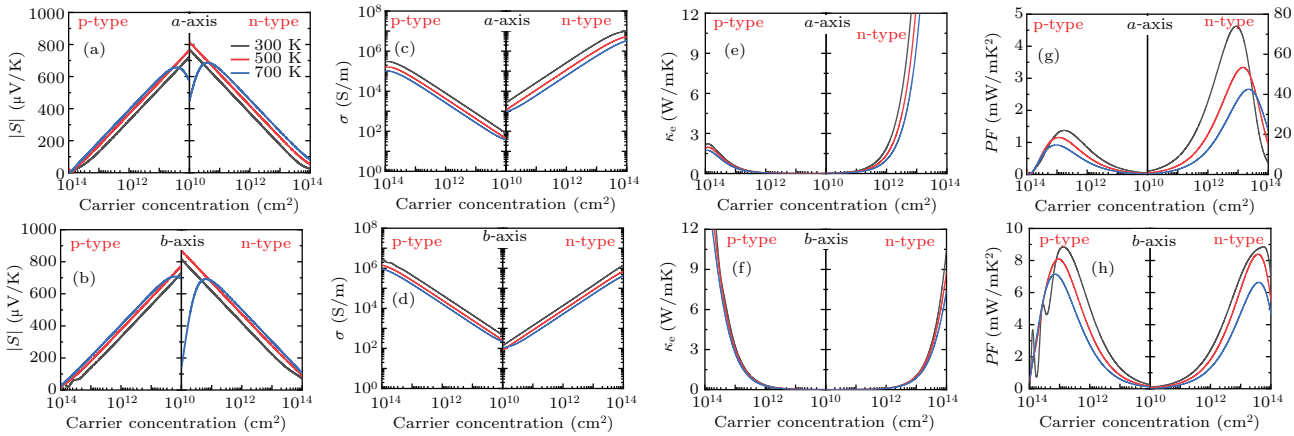


Fig. 4. Calculated thermoelectric parameters of Mo_2SCl_2 monolayer at different temperatures and carrier concentrations. The p-type (a) and n-type (b) Seebeck coefficient *S*. The p-type (c) and n-type (d) carrier conductivity σ. The p-type (e) and n-type (f) electronic thermal conductivity κ_e, the p-type (g) and n-type (h) power factor, *PF*.

In Fig. 5(a), Mo_2SCl_2 monolayer is taken as an example to calculate its detailed phonon dispersion and phonon density of states. It is found that, (i) high-frequency vibrations (> 8 THz) are mainly contributed by the covalent Mo–S bondings. (ii) Mo–Cl bondings give rise to vibrations at about 4.5 THz–8.5 THz. (iii) Acoustic phonons that originate from high ionic Cl and Mo ions exhibit weak dispersions. As a result, sound velocity in Mo_2SCl_2 monolayer is relatively low. (iv) The three acoustic modes (TA, ZA, and LA) show direction-dependent dispersions, indicating different sound velocities along the *a* and *b* directions. Anisotropies in lattice thermal conductivity and thermoelectric performance are predicted. (v) Large amount of low-frequency optical vibrations (1.0 THz–4.0 THz) are flat and mainly contributed by Mo atoms with minor contribution of Cl atoms, which correspond to the relative weak d–d bondings of Mo atoms. Additionally, LA and TA phonon modes at the high-symmetry *S* and *X* points become softened. The thermal conductivity along the *a* and *b* directions will be significantly reduced by these soft modes. Furthermore, these phonon modes show weak dispersions, indicating corresponding vibrations are highly localized and introducing the nearly zero-velocity optical phonon modes. These existing low-frequency localized vibrations have significant contribution to the reduced thermal conductivity.

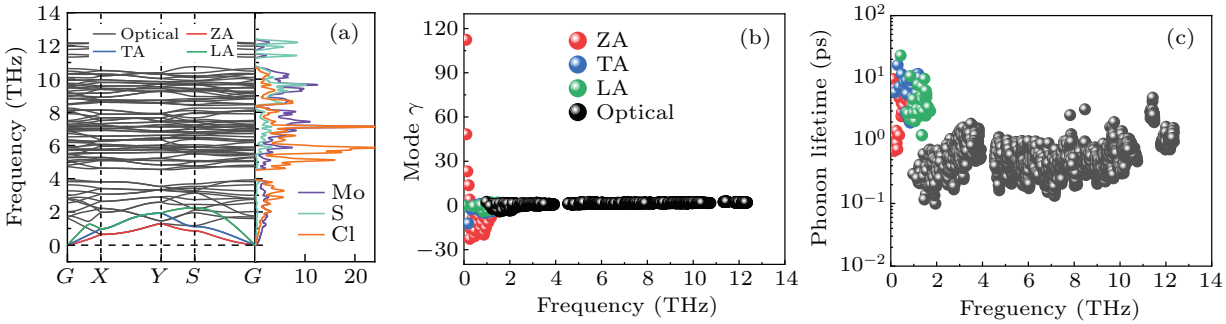


Fig. 5. (a) Phonon dispersions and phonon density of states of Mo_2SCl_2 monolayer. (b) Calculated Grüneisen parameters, γ, of three acoustic phonon modes and optical phonon modes of Mo_2SCl_2 monolayer at 300 K. (c) The phonon relaxation time of acoustic and optical phonons of various frequencies at 300 K.

In addition to the phonon frequency, anharmonicity featured by the Grüneisen parameter, is another important factor in lattice thermal conductivity. In Fig. 5(b), Grüneisen parameters of the three acoustic and optical modes are calculated. Our results reveal that ZA modes have large Grüneisen parameters, which means that strong anharmonicity exists, while Grüneisen parameters for LA, TA, and optical modes are much smaller. The strong phonon anharmonicity enhances phonon

scattering and greatly reduces thermal conductivity. Further support for the low thermal conductivity of Mo_2SCl_2 monolayer comes from the phonon lifetime calculations, as shown in Fig. 5(c). It is revealed that the acoustic modes exhibit much longer lifetimes than optical modes, implying the major roles in the thermal conductivity. Specifically, all the three acoustic phonon have low lifetimes ($\sim$ 10 ps) compared to other results,[29–31] which results in low thermal conductivity.

Then we turn to calculate the lattice thermal conductivity at 300 K, κ_l, of Mo_2SCl_2 monolayer, as shown in Fig. 6(a). It is found that κ_l decreases with temperature. At the room temperature ($T = 300$ K), Mo_2SCl_2 monolayer obtains rather low κ_l of 1.14 $W{\cdot}m^{-1}{\cdot}K^{-1}$ for the a direction and 2.29 $W{\cdot}m^{-1}{\cdot}K^{-1}$ for the b direction, respectively. Figure 6(b) shows the cumulative lattice thermal conductivity along both directions. It is revealed that the acoustic modes make major contribution (75% for the a direction and 69% for the b direction) to κ_l. Optical phonon with high frequencies have more influence on the thermal conductivity in the b direction. The phonon frequency ω_i is proportional to the sound velocity in the long-wave limit (or at the center of BZ). Actually, the phonon group velocity indicates the strength of interatomic bonding. In Fig. 6(c), the phonon group velocity, V_g, along the a and b directions are calculated. In the high-frequency range, V_g along the b direction is a larger than that along the a direction. While for low-frequency vibration modes, V_g of b direction are slightly smaller than that of the a direction due to the direct d–d coupling along the b direction. Therefore, κ_l in the b direction is significantly influenced by high-frequency optical modes and is improved by the high V_g, despite its small phonon lifetime. Further insights into the anisotropic thermal conduction can be acquired by the calculation of phonon mean free path (MFP), as shown in Fig. 6(d). The MFPs for the a-axis and b-axis phonons are 52.04 nm and 132.75 nm, respectively. Longer phonon MFP along the b direction than that along the a direction indicates reduced phonon scattering rate and enhanced thermal conductivity along this direction, which is consistent with the results in Fig. 6(a). These results confirm anisotropic and excellent thermoelectric properties of Mo_2AB_2 monolayers.

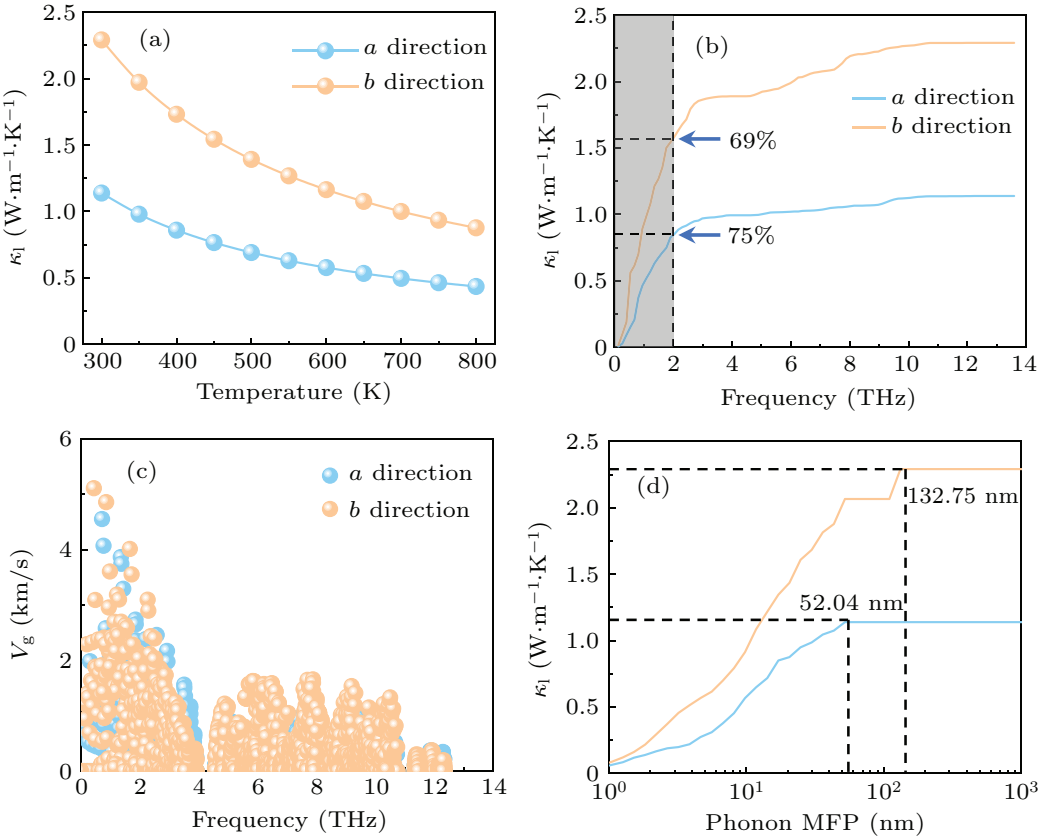


Fig. 6. (a) The lattice thermal conductivity κ_l of Mo_2SCl_2 monolayer as a function of temperature. (b) Cumulative lattice thermal conductivity and (c) phonon group velocity along a and b directions. The grey area in panel (b) represents the frequency range where acoustic modes make major contributions. (d) The variation of cumulative κ_l *versus* phonon mean free path for two directions. Temperature is set as $T = 300$ K in panels (b)–(d).

As expected, good anisotropic thermoelectric properties of Mo_2SCl_2 monolayer are confirmed by the calculated thermoelectric figure of merit, ZT, in Figs. 7(a) and 7(b). For the case of p-type carriers, ZT in the b direction is slightly higher than that in the a direction. While for the case of n-type carriers, the situations are just the reverse. In the b direction, ZTs of n-type and p-type Mo_2SCl_2 show rather similar variations with carrier density. The maximum ZTs at 300 K

are 0.71 for p-type Mo_2SCl_2 in the *b* direction and 3.61 for n-type Mo_2SCl_2 in the *a* direction. Moreover, *ZT*s for both n-type and p-type can be significantly improved by increasing the temperature. The n-type Mo_2SCl_2 monolayer exhibits a very high *ZT* larger than 5 at 700 K along the *a* direction.

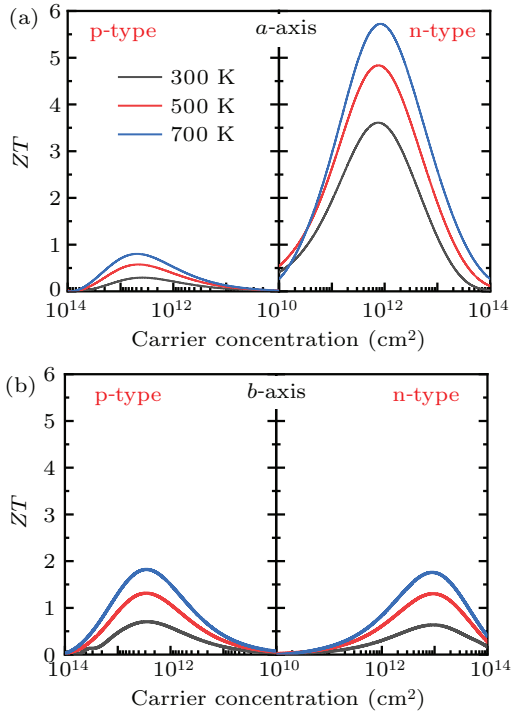


Fig. 7. Variations of the thermoelectric figure of merit (*ZT*) in the *a* direction (a) and *b* direction (b) of Mo_2SCl_2 monolayer as functions of carrier density.

4. Conclusions

In this paper, we employed first-principles approach to explore the electric and thermal transport properties of layered Mo_2AB_2 (A = S, Se, Te; B = Cl, Br, I) materials. Our results reveal that Mo_2AB_2 monolayers can be excellent thermoelectric materials with high electric conductivity σ and figures of merit *ZT*. The low lattice thermal conductivities, κ_l, originate from strong anharmonicities of ZA mode. Direct d–d couplings between Mo atoms, which introduce low-frequency phonon modes, further reduce κ_l and improve thermoelectric performance. Furthermore, the direction-dependent Mo–*A* bonding and Mo d–Mo d couplings have significant influence on the anisotropies in anharmonicities and transport properties. The thermoelectric properties of Mo_2AB_2 monolayers depend strongly on crystal orientation and carrier density. These results provide rigorous understanding on thermoelectric properties of double-anions compounds and can be very beneficial for designing materials with good thermoelectric performance.

Acknowledgements

Project supported by the Science and Technology Program of Guangzhou City (Grant Nos. 202102020389 and 202103030001), the Fund of Guangdong Provincial Key Laboratory of Information Photonics Technology (Grant No. 2020B121201011), and the National Natural Science Foundation of China (Grant Nos. 11804058 and 12064027). We also thank the Center of Campus Network & Modern Educational Technology, Guangdong University of Technology, Guangdong, China, for providing computational resources and technical support for this work.

References

[1] Shi X L, Chen W Y, Zhang T, Zou J and Chen Z G 2021 *Energ. Environ. Sci.* **14** 729
[2] Haque M A, Kee S, Villalva D R, Ong W L and Baran D 2020 *Adv. Sci.* **7** 1903389
[3] Li D L, Gong Y N, Chen Y X, Lin J M, Khan Q, Zhang Y P, Li Y, Zhang H and Xie H P 2020 *Nanomicro. Lett.* **12** 36
[4] Beretta D, Neophytou N, Hodges J M, Kanatzidis M G, Narducci D, Martin-Gonzalez M, Beekman M, Balke B, Cerretti G, Tremel W, Zevalkink A, Hofmann A I, Müller C, Dörling B, Campoy-Quiles M and Caironi M 2019 *Mater. Sci. Eng. R Rep.* **138** 100501
[5] Zevalkink A, Smiadak D M, Blackburn J L, Ferguson A J, Chabinyc M L, Delaire O, Wang J, Kovnir K, Martin J, Schelhas L T, Sparks T D, Kang S D, Dylla M T, Snyder G J, Ortiz B R and Toberer E S 2018 *Appl. Phys. Rev.* **5** 021303
[6] Vu T V, Nguyen C V, Phuc H V, Lavrentyev A A, Khyzhun O Y, Hieu N V, Obeid M M, Rai D P, Tong H D and Hieu N N 2021 *Phys. Rev. B* **103** 085422
[7] Li W, Zheng L L, Ge B H, Lin S Q, Zhang X Y, Chen Z W, Chang Y J and Pei Y Z 2017 *Adv. Mater.* **29** 1605887
[8] Liu W, Tan X J, Yin K, Liu H J, Tang X F, Shi J, Zhang Q J and Uher C 2012 *Phys. Rev. Lett.* **108** 166601
[9] Pei Y Z, Wang H and Snyder G J 2012 *Adv. Mater.* **24** 6125
[10] Zhai J Z, Wang T, Wang H C, Su W B, Wang X, Chen T T and Wang C L 2018 *Chin. Phys. B* **27** 047306
[11] Sun M, Tang G W, Wang H F, Zhang T, Zhang P Y, Han B, Yang M, Zhang H, Chen Y C, Chen J, Zhu Q F, Li J Y, Chen D D, Gan J L, Qian Qi and Yang Z M 2022 *Adv. Mater.* **34** 2202942
[12] Yang Q X, Lyu T, Nan B H, Tie J and Xu G Y 2022 *ACS Appl. Mater. Interfaces* **14** 32236
[13] Fan Y J, Peng K L, Huang Y L, Liao H J, Huang Z Y, Li J, Yan Y C, Gu H S, Zhang B, Hu Y M, Lu X and Zhou X Y 2022 *Rare Met.* **41** 3466
[14] Wang H, Chen J, Lu T Q, Zhu K, Li S, Liu J and Zhao H Z 2018 *Chin. Phys. B* **27** 047212
[15] Zhao K P, Zhu C X, Qiu P F, Blichfeld A B, Eikeland E, Ren D, Iversen B B, Xu F F, Shi X and Chen L D 2017 *Nano Energy* **42** 43
[16] Adam A M, Diab A K, El-Hadek M A, Sayed A O and Ibrahim E M M 2022 *J. Alloys Compd.* **920** 165952
[17] He W, Wang D, Wu H, Xiao Y, Zhang Y, He D, Feng Y, Hao Y J, Dong J F, Chetty R, Hao L, Chen D, Qin J, Yang Q, Li X, Song J M, Zhu Y, Xu W, Niu C, Li X, Wang G, Liu C, Ohta M, Pennycook S J, He J, Li J F and Zhao L D 2019 *Science* **365** 1418
[18] Wang R F, Dai L, Yan Y C, Peng K L, Lu X, Zhou X Y and Wang G Y 2018 *Chin. Phys. B* **27** 067201
[19] Ogunbunmi M O, Baranets S and Bobev S 2022 *Inorg. Chem.* **61** 10888
[20] Snyder G J and Toberer E S 2008 *Nat. Mater.* **7** 105
[21] Yang K K, Xiao J, Ren Z H, Wei Z M, Luo J W, Wei S H and Deng H X 2021 *J. Phys. Chem. Lett.* **12** 7832
[22] Dolyniuk J A, Owens-Baird B, Wang J, Zaikina J V and Kovnir K 2016 *Mater. Sci. Eng. R Rep.* **108** 1
[23] Ying P J, Li X, Wang Y C, Yang J, Fu C G, Zhang W Q, Zhao X B and Zhu T J 2017 *Adv. Funct. Mater.* **27** 1604145
[24] Qiu W J, Xi L L, Wei P, Ke X Z, Yang J H and Zhang W Q 2014 *Proc. Natl. Acad. Sci. USA* **111** 15031
[25] Wan B, Gao Z B, Huang X C, Yang Y Q, Chen L C, Wang Q Q, Fang C, Shen W X, Zhang Y W, Ma H A, Gou H Y, Jia X P and Zhang Z F 2022 *ACS Appl. Energy Mater.* **5** 9549
[26] Pal K, Xia Y, He J G and Wolverton C 2019 *Phys. Rev. Mater.* **3** 085402
[27] Wang N, Li M L, Xiao H Y, Gong H F, Liu Z J, Zu X T and Qiao L 2019 *Phys. Chem. Chem. Phys.* **21** 15097

[28] Hor Y S, Richardella A, Roushan P, Xia Y, Checkelsky J G, Yazdani A, Hasan M Z, Ong N P and Cava R J 2009 *Phys. Rev. B* **79** 195208

[29] Qi H B, Sun Z H, Shen C, Chang Z, Wang Z S, Wang X P, Zhang M and Wang N 2022 *ACS Appl. Energy Mater.* **5** 7371

[30] Fan Q, Yang J H, Qi H B, Yu L F, Qin G Z, Sun Z H, Shen C and Wang N 2022 *Phys. Chem. Chem. Phys.* **24** 11268

[31] Chang Z, Liu K, Sun Z H, Yuan K P, Cheng S W, Gao Y F, Zhang X L, Shen C, Zhang H B, Wang N and Tang D W 2022 *Int. J. Extrem. Manuf.* **4** 025001

[32] Liao H J, Xiao Y, Yang Y B, Huang L, Dong H F and Wu F G 2022 *Phys. Rev. B* **105** 195427

[33] Kresse G and Furthmuller J 1996 *Phys. Rev. B* **54** 11169

[34] Kresse G and Joubert D 1999 *Phys. Rev. B* **59** 1758

[35] Perdew J P, Burke K and Ernzerhof M 1996 *Phys. Rev. Lett.* **77** 3865

[36] Deringer V L, Tchougreeff A L and Dronskowski R 2011 *J. Phys. Chem. A* **115** 5461

[37] Nelson R, Ertural C, George J, Deringer V L, Hautier G and Dronskowski R 2020 *J. Comput. Chem.* **41** 1931

[38] Heyd J and Scuseria G E 2004 *J. Chem. Phys.* **121** 1187

[39] Jia W L, Cao Z Y, Wang L, Fu J Y, Chi X B, Gao W G and Wang L W 2013 *Comput. Phys. Commun.* **184** 9

[40] Jia W L, Fu J Y, Cao Z Y, Wang L, Chi X B, Gao W G and Wang L W 2013 *J. Comput. Phys.* **251** 102

[41] Baroni S, De Gironcoli S, Dal Corso A and Giannozzi P 2001 *Rev. Mod. Phys.* **73** 515

[42] Chaput L, Togo A, Tanaka I and Hug G 2011 *Phys. Rev. B* **84** 094302

[43] Togo A and Tanaka I 2015 *Scripta Materialia* **108** 1

[44] Li W, Carrete J, Katcho A N and Mingo N 2014 *Comput. Phys. Commun.* **185** 1747

[45] Madsen G K H and Singh D J 2006 *Comput. Phys. Commun.* **175** 67

[46] Tan G J, Shi F Y, Doak J W, Sun H, Zhao L D, Wang P L, Uher C, Wolverton C, Dravid V P and Kanatzidis M G 2015 *Energ. Environ. Sci.* **8** 267

[47] Pei Y Z, Lalonde A, Iwanaga S and Snyder G J 2011 *Energ. Environ. Sci.* **4** 2085

[48] Ahmad S and Mahanti S D 2010 *Phys. Rev. B* **81** 165203